Subwavelength Acoustic Vortex Beams Using Self-Demodulation

Noé Jiménez, Joao Ealo, Rubén Muelas-Hurtado, Aroune Duclos, Vicente Romero-García

Sub-wavelength acoustical vortex beams using self-demodulation

Noé Jiménez,[1,*] Joao Ealo,[2] Rubén D. Muelas-Hurtado,[2,3] Aroune Duclos,[4] and Vicent Romero-García[4]

[1] *Instituto de Instrumentación para Imagen Molecular (I3M), Universitat Politècnica de València - CSIC, València, Spain*
[2] *School of Mechanical Engineering, Universidad del Valle, Cali, Colombia*
[3] *School of Civil and Geomatic Engineering, Universidad del Valle, Cali, Colombia.*
[4] *Laboratoire d'Acoustique de l'Université du Mans (LAUM), UMR CNRS 6613, Institut d'Acoustique - Graduate School (IA-GS), CNRS, Le Mans Université, France*

Acoustic vortices with sub-wavelength dimensions and tunable topological charge are theoretically and experimentally synthesized at distances far beyond the Rayleigh diffraction length of the source using self-demodulation. A dual helical acoustic source is used to generate two primary confocal vortex beams at different frequencies and different topological charges. As a consequence of the conservation of angular momentum during nonlinear wave mixing, a self-demodulated vortex beam at the difference frequency emerges, keeping the spatial features of the primary vortex beams and a topological charge which is the difference of their topological charges. We report sub-diffractive vortices whose characteristic size is 18 times smaller than its wavelength at a distance 2.8 times the Rayleigh diffraction length. The generation and focusing of sub-wavelength vortices paves the way for long-range communication, biomedical and wave-matter interaction applications.

I. INTRODUCTION

The transfer of energy and momentum from acoustic and elastic waves to matter has been currently used to develop ground-breaking applications. Novel wave-matter interaction mechanisms have allowed emerging applications, e.g., the recent advances in neuroscience using thermal ablation of deep-brain nuclei with sub-millimetric precision [1], the mechanical interaction of focused ultrasound beams with tissues for non-invasive and localized neuromodulation [2], or targeted drug-delivery in the brain [3]. Interestingly, in addition to linear momentum, wave fields with spiral phase dislocations, i.e., acoustic vortices [4], carry orbital angular momentum. These acoustic vortices can transfer their angular momentum to solid objects and exert mechanical torques [5–8].

Vortex beams are characterized by a collimated wavefront with a phase dependence of the type $e^{il\phi}$, with ϕ the azimuthal angle and l the topological charge, respectively. At the principal axis of the vortex beam the field exhibits a phase singularity and the field is null. These singular fields can produce negative radiation forces on small particles, offering unique possibilities for manipulating matter [9]. Recently, they have received increasing interest mainly due to direct practical applications for particle trapping and manipulation [10–15]. Acoustic vortices can exert mechanical forces several orders of magnitude higher than those of their optical counterparts [16, 17] with reduced thermal effects. They have recently shown potential applications to manipulate individual cells without inducing photothermal and/or photochemical damages [18], to trap and guide kidney stones fragments [19], or to selectively guide individual drug-delivery carriers based on microbubbles [20].

In order to generate a vortex beam, a precise control of the acoustic field is required. Methods to synthesize these beams include active devices such as phased arrays [21–24], helical radiating surfaces [21, 25], spiral diffraction gratings following an Archimedes' spiral [26–28] to generate high order Bessel beams, Fresnel spiral diffraction gratings [29] to generate sharpy focused vortex beams, diverging [30] and converging [29, Supplementary material] Archimedean spirals, or active vibrating surfaces with spiral shape [31, 32]. A version of these active spirals are interdigitated transducers [33] whose spiralling shape can encode the phase of the field like a hologram and generate vortices through the generation of swirling Rayleigh waves [34]. The whole holographic information of a vortex can be encoded in an acoustic hologram, enabling the generation of high order Bessel beams with long depth of field in homogeneous media [35]. Acoustic holograms can also generate vortex beams through complex biological media, e.g., correcting the phase aberrations during transcranial propagation [36]. Acoustic vortices can also be generated by systems exploiting the photoacoustic effect [37]. Recently, metamaterials have been used to generate vortex beams by using flat and sub-wavelength structures [38–42], allowing a precise manipulation of the transmitted phase by tuning the geometry of the resonators at selected frequencies.

However, in all these configurations the natural diffraction of the wavefront limits the size of the vortex. For example, a high-order Bessel beam whose transversal pressure profile is described by a Bessel function of the first kind and order l, $p(r,\phi) = J_l(k_r r)\exp(il\phi)$, presents a minimum distance between pressure maxima of $D_{\min} \approx \lambda(|l| + 0.8086|l|^{1/3})/\pi$, where λ is the wavelength [27]. In this case, diffraction limits the minimum size of such vortices to $D_{\min} \approx 0.57\lambda$ for $l = 1$, and this value is only reached for distances smaller than the Rayleigh diffraction length of the source due to the divergence of the beam, given by S/λ where S is the surface of a circular-

* nojigon@upv.es; corresponding author

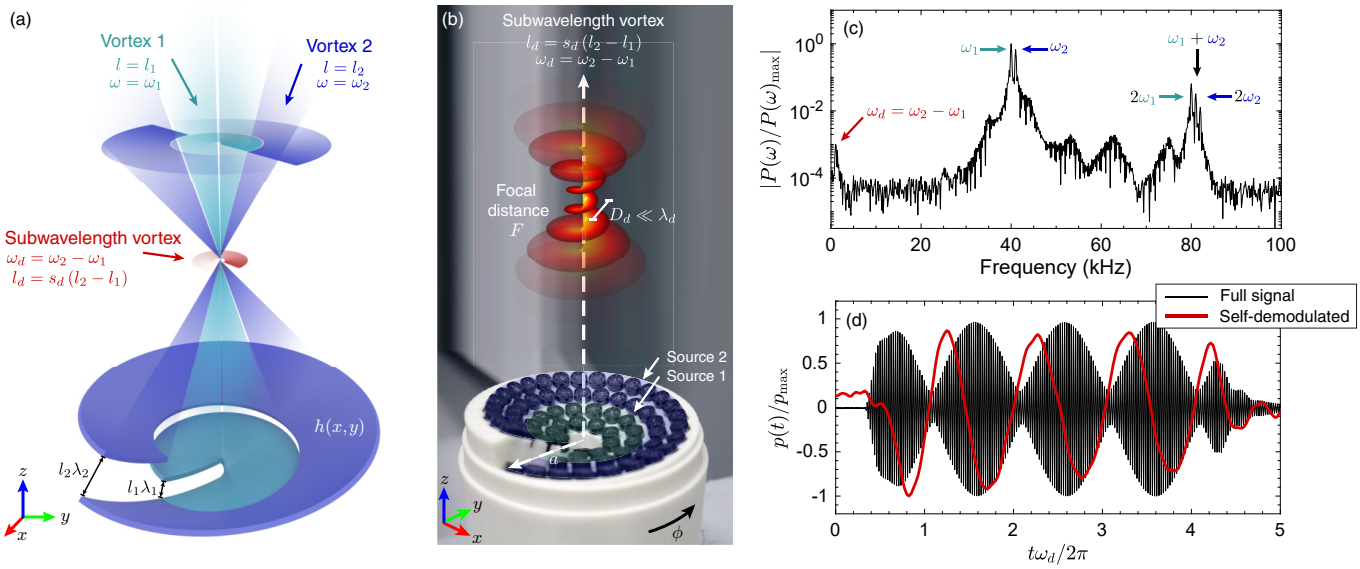

FIG. 1. (a) Scheme of the system composed of two confocal focused vortex beams at frequencies ω_1 and ω_2, with topological charges l_1 and l_2, respectively. Self-demodulation is generated by nonlinearity, producing a vortex at the difference frequency $\omega_d = \omega_2 - \omega_1$, with a topological charge of $l_d = l_2 - l_1$ and a beam-width given by D_d in the sub-wavelength regime. (b) Photograph of the helical source used in the experiments. (c) Measured spectrum at the focal spot showing the nonlinear generated harmonics by combination of the two primary vortex beams. (d) Corresponding temporal waveform and low-pass filtered signal (normalized). The maximum root-mean-square pressure was 138.4 Pa at 40 kHz.

aperture source. Recently, increasing attention has been paid to restoring the evanescent components of a field to overcome the diffraction limit either using metamaterials [43–45], or time-reversal techniques [46]. However, as these approaches rely on evanescent waves, their use is restricted to near-field distances.

Synthesizing a vortex of small size at low frequency can be of great interest to many practical applications. For example, in underwater communications using acoustic vortex transceivers [47–50], the size of the instrumentation for detection is of the order of the radius of the vortex. On the one hand, a mechanism to reduce the width of the vortex impinging in the detector should enhance the detected signal and improve the system sensibility and its performance [47]. On the other, when propagating at long distances in underwater applications, or in strongly scattering and absorbing media as the ocean floor, ultrasonic beams are strongly attenuated. In these cases, it is desirable to emit at low ultrasonic frequencies. However, by directly reducing the frequency of the ultrasonic source its directivity becomes very wide and, in addition it also has a negative impact on the source efficiency because radiation impedance decreases. A common solution is to use the self-demodulation effect to generate a parametric acoustic antenna [51]. These systems use two primary ultrasonic transducers radiating two overlapping narrow beams of high amplitude and different frequencies. The nonlinear mixing of the primary beams generates a new component at the difference frequency. This low-frequency beam is generated progressively along a long path, and its radiation pattern is similar to an *endfire* array, it interferes destructively at the transverse direction and constructively in the forward direction. Therefore, the self-demodulated beam conserves the directivity of the primary beams [52]. Parametric beams are commercially available and used for underwater communications, sub-bottom profilers or detection of buried targets. In this way, obtaining a parametric vortex antenna will be desirable to applications based on vortices such as underwater communications [47–50], propagation in inhomogeneous media [53] or imaging techniques based on vortices [54, 55].

Other application that should benefit from subwavelength vortices is particle trapping in biomedical ultrasound. It has been recently demonstrated that bubbles can be trapped using ultrasound beams and their payload can be delivered by exploiting its cavitation activity, the latter linked to the bubble resonance [20, 56]. Many drug-delivery carriers are based on coated microbubbles of small size, of the order of several micrometers [57]. In this way, a mechanism to control the trapping size, linked to the vortex diameter, and simultaneously tuning the excitation frequency, linked to the microbubble resonance, can be of great interest to design accurate drug-delivery applications. In addition, low-frequency vortices are more robust to phase aberrations when propagating in strongly refracting and absorbing tissues such as the skull bones [36, 58].

Obtaining vortices of tunable topological charge using nonlinearity was demonstrated first in Optics, e.g., by second harmonic generation using the nonlinear mixing of two beams and synthesized gratings [59] or frequency

doubling using a nonlinear crystal [60], where parametric frequency converter was demonstrated for vortex charge doubling. Later, sum-frequency generation was demonstrated using a nonlinear crystal and computer generated holograms [61, 62]. The frequency conversion enabled the realization of several light processors, including arithmetical operations with the topological charges of the interacting vortices. Later, these concepts were studied in Acoustics to synthesize vortices as a result of harmonic generation by frequency doubling [22, 23] and by the nonlinear mixing of two vortices [63], where the laws of conservation of orbital angular momentum were also provided. These studies were extended to nonlinear shock waves [64] and, lately, fractional vortices were identified in short pulsed helicoidal beams [65].

In this work, we synthesize a vortex beam of sub-wavelength size at a distance beyond Rayleigh diffraction length using the nonlinear mixing of two confocal, high-frequency and detuned vortex beams of different topological charges. We demonstrate the concept using the natural self-demodulation phenomenon in air. We generate a focused vortex beam of integer topological charge whose distance between magnitude maxima is ~ 18 times smaller than its wavelength at a distance ~ 2.8 times the Rayleigh diffraction length.

II. METHODS

A device was manufactured by disposing 10-mm diameter ultrasound emitters operating in air over two different helical surfaces as shown in Figs. 1(a-b). The helical profile of the n-th surface (with $n = 1, 2$) was designed to generate a focused beam at a focal point, $\mathbf{r}(\phi, r, z) = (0, 0, F)$, and, simultaneously, produce at this location a difference of time of flight equal to $\Delta t_n = l_n \phi/\omega_n$, where l_n is the topological charge of the n-th primary vortex beam, ω_n the angular frequency and ϕ the azimuthal coordinate [66]. In particular, the first source, composed of the two internal concentric rings of transducers, see Fig. 1(b), was excited with a sinusoidal pulse burst of $\omega_1/2\pi = 40$ kHz while the second one, composed of the two external concentric rings of transducers, was excited at $\omega_2/2\pi = 41$ kHz. The topological charges of the primary vortex beams, defined by the curvature of the helical surfaces, were set to $l_1 = 1$ and $l_2 = 2$. Source aperture was set to $2a = 110$ mm, with a the radius of the source, and the focal point was $F = 100$ mm. Thus, the Rayleigh distances for the primary vortex beams are around $\pi a^2/\lambda_1 \approx \pi a^2/\lambda_2 \approx 1.1$ m.

For finite-amplitude waves, and when all emitters are active, both beams interact and due to material and advective nonlinearity wave mixing occurs during propagation. Higher harmonics arise as arithmetical combinations of the fundamental waves of both beams, as it is shown in the spectrum plotted in Fig. 1(c), acquired at the focal spot. The root-mean-square pressure measured was 138.4 Pa at 40 kHz (a sound pressure level of 136.8 dB referenced at 20 μPa), enough to trigger weak nonlinear effects. In addition to higher harmonics, a difference-frequency mode of frequency $\omega_d = \omega_2 - \omega_1$ was generated due to the nonlinear self-demodulation of the beating wavefront, as shown in Fig. 1(d).

As homogeneous acoustic media lack of strong dispersion, phase-matching holds during nonlinear propagation and harmonic generation processes are cumulative with distance. On the one hand, it is expected that the locally-generated self-demodulated mode presents a field spatial distribution similar to those of the primary beams, as occurs in parametric acoustic antennas [51]. On the other hand, the phase of the self-demodulated beam depends on the spatio-temporal interference of the two vortex beams, which is linked to their topological charges [67]. This results in a self-demodulated beam with a phase factor $\exp(il_d\phi)$ where the topological charge of the self-demodulated beam is

$$l_d = s_d(l_2 - l_1), \tag{1}$$

where $s_d = \text{sign}(\omega_2 - \omega_1)$, due to the conservation of topological charge of nonlinear vortices, which is indeed a consequence of the conservation of angular momentum [22]. Particular attention should be paid to Eq. (1) because this is not valid if the frequencies of the primary beams are commensurable [63]. However, in self-demodulation applications, this is usually fulfilled as the primary beams are commonly chosen with nearby frequencies. Therefore, to synthesize a sub-wavelength vortex by self-demodulation, the primary beams should present different topological charges and frequencies and, in addition, their field distribution must overlap in space.

III. RESULTS

The field generated by each of the two confocal nonlinear vortices is shown in Fig. 2. First, the acoustic field radiated by such a device in the linear regime is theoretically obtained using the Rayleigh-Sommerfeld diffraction integral [68]. The results for small-amplitude waves, presented in Figs. 2(a-c), show that the helical source correctly generates the focused vortex beams at frequencies ω_1 and ω_2. However, if the source is excited at ω_d, as $k_d a \ll 1$ the value of Rayleigh diffraction length is very low and the field decays fast due to spherical spreading.

A. Nonlinear vortex generation

A simulation was performed by solving the nonlinear Westervelt's equation [51] in a retarded coordinate frame using a spectral operator-splitting method and including thermoviscous absorption [69]. This method allows the numerical integration of wide-aperture sources beyond the parabolic approximation. The boundary conditions were calculated by integrating the field radiated by each

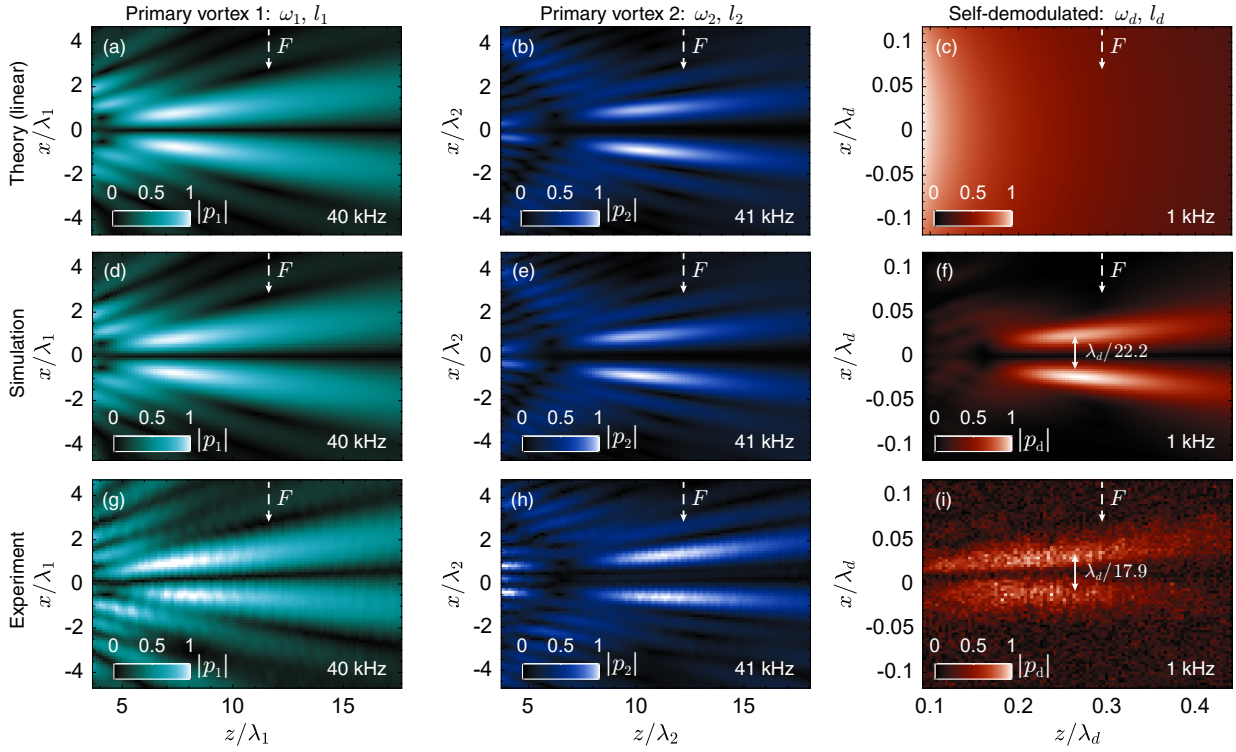

FIG. 2. Sagittal field cross-section at $y = 0$, obtained by (a-c) linear theory, (d-f) nonlinear simulation and (g-i) experiment, showing the magnitude of the acoustic field at frequencies 40 kHz, 41 kHz and 1 kHz, respectively. The maximum root-mean-square pressure was 138.4 Pa at 40 kHz.

of the transducers of the helical phased-array source over a plane located at $z = 3$ cm using the linear Rayleigh-Sommerfeld integral [70]. Then, nonlinear effects are accounted for, and the field is integrated along the axial coordinate. In addition, experiments were conducted in a semi-anechoic environment. The emitters on the helical surfaces were excited with sinusoidal pulse-burst signals of length $t = 8\pi/\omega_d$ and the field was scanned by a pinhole-microphone using a 3D positioning system. Simulated and experimental results are shown in Figs. 2(d-f) and Figs. 2(g-i), respectively. First, due to a weakly nonlinear propagation, the nonlinear simulated field of each of the primary vortex beams, Figs. 2(d-e), agrees the theoretical linearly-diffracted pattern, Figs. 2(a-b). The corresponding experimental fields, Figs. 2(g-h), agree the theoretical ones. The weakly-oscillating pattern in the axial direction indicates the presence of a weak counter-propagating mode caused by reflections on the positioning system. We note that the location of the pressure maxima does not correspond to the focus due to strong diffraction effects of the small-aperture source.

In addition, the self-demodulated component for the simulation and experiment is respectively shown in Figs. 2(f) and 2(i). A low-frequency beam at $\omega_d = 1$ kHz is generated locally, and its spatial distribution matches the overlapping volume of the two primary beams. Its corresponding wavelength is $\lambda_d = 2\pi c_0/\omega_d \gg \lambda_n$, therefore, the width of the beam, dominated by the width of the primary beams, is deep sub-wavelength.

B. Sub-diffractive vortices

The transversal cross-sections at the plane $\mathbf{r}(x, y, z) = (x, y, F)$ corresponding to the cases analysed in Fig. 2 are shown in Fig. 3. First, the theoretical field distributions of the primary beams calculated in the linear regime are shown in Figs. 3(a-d). The helical source correctly generates a focused vortex with topological charge $l_1 = 1$ and $l_2 = 2$, respectively, and the field vanishes at the phase singularity. However, the linear propagation of a 1 kHz wave does not present such a phase dislocation [Figs. 3(e-f)]. In addition, as F is much bigger than the Rayleigh diffraction length for 1 kHz, $S/\lambda_d \approx F/3.6 = 2.8$ cm, strong diffraction dominates the propagation and this low-frequency beam cannot be collimated.

In the nonlinear regime, the magnitude and the phase distributions of the two primary vortex beams, shown in Figs. 3 (g-j) and 3 (m-p) for simulations and measurements respectively, also confirm the formation of a focused helical beam. The simulations and experiments are in good agreement, only small discrepancies are observed for transverse pattern of the 41-kHz primary beam in the measurements. The self-demodulated vortex arises as a result of the nonlinear mixing of the two primary vortex beams [Figs. 3(k,l) and 3(q,r) for simulations and exper-

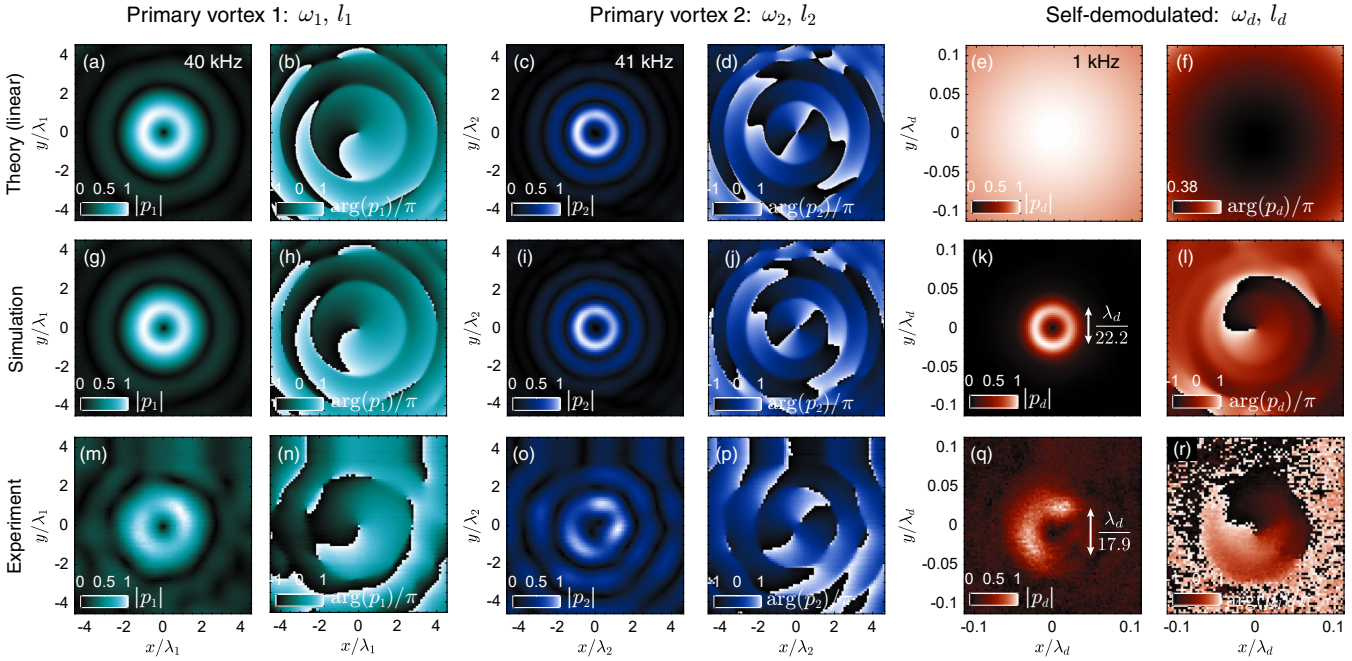

FIG. 3. Transverse field cross-section at $z = 80$ mm, obtained by (a-f) linear theory, (g-l) nonlinear simulation and (m-r) experiment, showing the normalized magnitude ($|p_1|$) and the normalized phase ($\arg(p_1)/\pi$) of the acoustic field at frequencies 40 kHz, 41 kHz and 1 kHz, respectively. The maximum root-mean-square pressure was 138.4 Pa at 40 kHz.

iments, respectively]. Its topological charge is given by $l_d = l_2 - l_1 = 1$, showing the conservation of topological charge and, therefore, the conservation of orbital angular momentum during the nonlinear mixing of the primary beams as given by Eq. (1).

Figure 4 shows the transversal pressure-field distribution of the self-demodulated vortex beam at $z = 80$ mm and $y = 0$ mm. The width of the vortex, D_d, is 17.9 times smaller than the wavelength in the experimental observations ($D_d = \lambda_d/22.2$ in simulations). Note that the measurement distance is 2.8 times the Rayleigh diffraction length for the self-demodulated mode. The field at the axis ($x = 0$) becomes null due to the phase singularity. The phase of the beam along the azimuthal coordinate ϕ, depicted in Fig. 4(b), agrees with a linear profile of $(l_2 - l_1)\phi = l_d\phi$, demonstrating the topological charge conservation during nonlinear mixing. Using this approach, vortices of arbitrary topological charge and size can be synthesized by tuning the parameters of the primary beams [71].

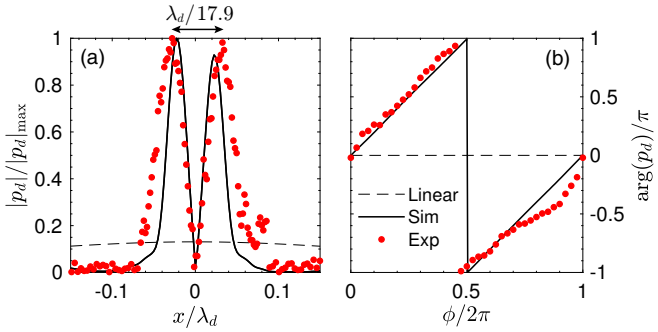

FIG. 4. (a) Normalized field magnitude cross-section $p(x, 0, 80\text{ mm})$ at 1 kHz (difference frequency) obtained experimentally (markers), numerically (continuous) and by linear theory (dashed). (b) Phase of the self-demodulated field along the azimuthal coordinate.

IV. CONCLUSIONS

In this work we have shown the sub-wavelength and sub-diffractive generation of acoustic vortices at distances beyond Rayleigh diffraction length by using the nonlinear self-demodulation. To generate vortices below the diffraction limit by self-demodulation, the primary vortex beams should present different topological charge and frequency, and their field distribution must overlap in space. Sub-wavelength vortices emerge as a result of the spatio-temporal interference of two primary vortex beams due to the conservation of angular momentum during nonlinear wave-mixing.

Synthesizing vortices below the diffraction limit is of great interest for many applications such as underwater acoustic communications using vortex-transceivers [47]. As ocurrs in parametric acoustic antennas, sub-wavelength vortices are generated all along the *end-fire* virtual array formed by the primary beams. Therefore, self-demodulated vortices should conserve the radiation pattern of the primary beams because at transverse direction they interfere destructively. However, the energy is

transmitted at the difference frequency. For this reason, vortex-encoded information using self-demodulated vortex beams can be transmitted at higher distances due to lower absorption and scattering when travelling in complex media.

Moreover, using standard vortices the trapping size is linked to the frequency of the beam and the topological charge. By self-demodulation, the size of the vortex can be tuned by the primary frequencies, while the frequency is a free parameter that depends on the detuning of the primary beams. This mechanism enables a degree of freedom to control and manipulate resonating particles such as bubbles or coated microbubbles. In this case, the trap allows the manipulation while by tuning the difference frequency one can control the cavitation activity, the latter linked by the resonance of the target. In the context of biomedical ultrasound applications, controlling the cavitation activity of trapped microbubbles is useful to design drug-delivery carriers to deliver the payload of the resonating therapeutic agent. Miniaturization [72] of the proposed concept can be performed either using helical surfaces, holograms, spiral diffraction gratings or a pair of coiled spiral sources.

These results show that vortices of arbitrary topological charge with tunable and subwavelength width can be generated using self-demodulation, paves the way for practical applications like long-range underwater communication systems based on vortex transceivers, or trapping and manipulating particles and microbubbles for biomedical ultrasound applications.

ACKNOWLEDGMENTS

This research has been supported by the Spanish Ministry of Science, Innovation and Universities through grants "Juan de la Cierva - Incorporación" IJC2018-037897-I and PID2019-111436RB-C22, by the Agència Valenciana de la Innovació through grants INNVA1/2020/92 and INNCON/2021/8, and by the project HYPERMETA funded under the program Étoiles Montantes of the Région Pays de la Loire. R.D.M.-H acknowledges support from Colciencias Scholarship program No. 727-2015.

[1] W. J. Elias, D. Huss, T. Voss, J. Loomba, M. Khaled, E. Zadicario, R. C. Frysinger, S. A. Sperling, S. Wylie, S. J. Monteith, *et al.*, A pilot study of focused ultrasound thalamotomy for essential tremor, N. Engl. J. Med. **369**, 640 (2013).

[2] Y. Tufail, A. Yoshihiro, S. Pati, M. M. Li, and W. J. Tyler, Ultrasonic neuromodulation by brain stimulation with transcranial ultrasound, Nat. Protoc. **6**, 1453 (2011).

[3] N. Lipsman, Y. Meng, A. J. Bethune, Y. Huang, B. Lam, M. Masellis, N. Herrmann, C. Heyn, I. Aubert, A. Boutet, *et al.*, Blood–brain barrier opening in Alzheimer's disease using MR-guided focused ultrasound, Nat Commun **9**, 1 (2018).

[4] J. Nye and M. Berry, Dislocations in wave trains, in *Proc. Math. Phys. Eng. Sci.*, Vol. 336 (The Royal Society, 1974) pp. 165–190.

[5] K. Volke-Sepúlveda, A. O. Santillán, and R. R. Boullosa, Transfer of angular momentum to matter from acoustical vortices in free space, Phys. Rev. Lett. **100**, 024302 (2008).

[6] A. Anhäuser, R. Wunenburger, and E. Brasselet, Acoustic rotational manipulation using orbital angular momentum transfer, Phys. Rev. Lett. **109**, 034301 (2012).

[7] C. E. Demore, Z. Yang, A. Volovick, S. Cochran, M. P. MacDonald, and G. C. Spalding, Mechanical evidence of the orbital angular momentum to energy ratio of vortex beams, Phys. Rev. Lett. **108**, 194301 (2012).

[8] Z. Hong, J. Zhang, and B. W. Drinkwater, Observation of orbital angular momentum transfer from bessel-shaped acoustic vortices to diphasic liquid-microparticle mixtures, Phys. Rev. Lett. **114**, 214301 (2015).

[9] P. L. Marston, Radiation force of a helicoidal Bessel beam on a sphere, Jour. Acous. Soc. Am. **125**, 3539 (2009).

[10] J. Wu, Acoustical tweezers, Jour. Acous. Soc. Am. **89**, 2140 (1991).

[11] D. Baresch, J.-L. Thomas, and R. Marchiano, Observation of a single-beam gradient force acoustical trap for elastic particles: acoustical tweezers, Phys. Rev. Lett. **116**, 024301 (2016).

[12] A. Marzo, M. Caleap, and B. W. Drinkwater, Acoustic virtual vortices with tunable orbital angular momentum for trapping of Mie particles, Phys. Rev. Lett. **120**, 044301 (2018).

[13] Z. Gong and M. Baudoin, Particle assembly with synchronized acoustic tweezers, Phys. Rev. Appl **12**, 024045 (2019).

[14] X.-D. Fan and L. Zhang, Trapping force of acoustical bessel beams on a sphere and stable tractor beams, Physical Review Applied **11**, 014055 (2019).

[15] C. R. Courtney, B. W. Drinkwater, C. E. Demore, S. Cochran, A. Grinenko, and P. D. Wilcox, Dexterous manipulation of microparticles using Bessel-function acoustic pressure fields, Appl. Phys. Lett. **102**, 123508 (2013).

[16] A. Ashkin, Acceleration and trapping of particles by radiation pressure, Phys. Rev. Lett. **24**, 156 (1970).

[17] D. G. Grier, A revolution in optical manipulation, Nature **424**, 810 (2003).

[18] M. Baudoin, J.-L. Thomas, R. Al Sahely, J.-C. Gerbedoen, Z. Gong, A. Sivery, O. B. Matar, N. Smagin, P. Favreau, and A. Vlandas, Spatially selective manipulation of cells with single-beam acoustical tweezers, Nat. Commun. **11**, 1 (2020).

[19] M. A. Ghanem, A. D. Maxwell, Y.-N. Wang, B. W. Cunitz, V. A. Khokhlova, O. A. Sapozhnikov, and M. R. Bailey, Noninvasive acoustic manipulation of objects in a living body, Proc. Natl. Acad. Sci. U.S.A. (2020).

[20] D. Baresch and V. Garbin, Acoustic trapping of microbubbles in complex environments and controlled pay-

load release, Proc. Natl. Acad. Sci. U.S.A. **117**, 15490 (2020).
[21] B. T. Hefner and P. L. Marston, An acoustical helicoidal wave transducer with applications for the alignment of ultrasonic and underwater systems, Jour. Acous. Soc. Am. **106**, 3313 (1999).
[22] J.-L. Thomas and R. Marchiano, Pseudo angular momentum and topological charge conservation for nonlinear acoustical vortices, Phys. Rev. Lett. **91**, 244302 (2003).
[23] R. Marchiano and J.-L. Thomas, Synthesis and analysis of linear and nonlinear acoustical vortices, Phys. Rev. E **71**, 066616 (2005).
[24] J. F. Pazos-Ospina, J. L. Ealo, and E. E. Franco, Characterization of phased array-steered acoustic vortex beams, Jour. Acous. Soc. Am. **142**, 61 (2017).
[25] J. L. Ealo, J. C. Prieto, and F. Seco, Airborne ultrasonic vortex generation using flexible ferroelectrets, IEEE Trans. Ultrason. Ferroelectr. Freq. Control **58**, 1651 (2011).
[26] N. Jiménez, V. Sánchez-Morcillo, R. Picó, L. Garcia-Raffi, V. Romero-Garcia, and K. Staliunas, High-order acoustic bessel beam generation by spiral gratings, Physics Procedia **70**, 245 (2015).
[27] N. Jiménez, R. Picó, V. Sánchez-Morcillo, V. Romero-García, L. M. García-Raffi, and K. Staliunas, Formation of high-order acoustic Bessel beams by spiral diffraction gratings, Phys. Rev. E **94**, 053004 (2016).
[28] T. Wang, M. Ke, W. Li, Q. Yang, C. Qiu, and Z. Liu, Particle manipulation with acoustic vortex beam induced by a brass plate with spiral shape structure, Appl. Phys. Lett. **109**, 123506 (2016).
[29] N. Jiménez, V. Romero-García, L. M. García-Raffi, F. Camarena, and K. Staliunas, Sharp acoustic vortex focusing by Fresnel-spiral zone plates, Appl. Phys. Lett. **112**, 204101 (2018).
[30] X. Jiang, J. Zhao, S.-l. Liu, B. Liang, X.-y. Zou, J. Yang, C.-W. Qiu, and J.-c. Cheng, Broadband and stable acoustic vortex emitter with multi-arm coiling slits, Appl. Phys. Lett. **108**, 203501 (2016).
[31] R. D. Muelas-Hurtado, J. L. Ealo, J. F. Pazos-Ospina, and K. Volke-Sepúlveda, Generation of multiple vortex beam by means of active diffraction gratings, Appl. Phys. Lett. **112**, 084101 (2018).
[32] R. D. Muelas-Hurtado, J. L. Ealo, and K. Volke-Sepúlveda, Active-spiral Fresnel zone plate with tunable focal length for airborne generation of focused acoustic vortices, Applied Physics Letters **116**, 114101 (2020).
[33] A. Riaud, M. Baudoin, O. B. Matar, L. Becerra, and J.-L. Thomas, Selective manipulation of microscopic particles with precursor swirling rayleigh waves, Physical Review Applied **7**, 024007 (2017).
[34] A. Riaud, J.-L. Thomas, E. Charron, A. Bussonnière, O. B. Matar, and M. Baudoin, Anisotropic swirling surface acoustic waves from inverse filtering for on-chip generation of acoustic vortices, Physical Review Applied **4**, 034004 (2015).
[35] S. Jiménez-Gambín, N. Jiménez, J. M. Benlloch, and F. Camarena, Generating bessel beams with broad depth-of-field by using phase-only acoustic holograms, Sci. Rep. **9**, 1 (2019).
[36] S. Jiménez-Gambín, N. Jiménez, and F. Camarena, Transcranial focusing of ultrasonic vortices by acoustic holograms, Physical Review Applied **14**, 054070 (2020).
[37] S. Gspan, A. Meyer, S. Bernet, and M. Ritsch-Marte, Optoacoustic generation of a helicoidal ultrasonic beam, Jour. Acous. Soc. Am. **115**, 1142 (2004).
[38] X. Jiang, Y. Li, B. Liang, J.-c. Cheng, and L. Zhang, Convert acoustic resonances to orbital angular momentum, Phys. Rev. Lett. **117**, 034301 (2016).
[39] L. Ye, C. Qiu, J. Lu, K. Tang, H. Jia, M. Ke, S. Peng, and Z. Liu, Making sound vortices by metasurfaces, AIP Adv. **6**, 085007 (2016).
[40] A. Marzo, A. Ghobrial, L. Cox, M. Caleap, A. Croxford, and B. Drinkwater, Realization of compact tractor beams using acoustic delay-lines, Appl. Phys. Lett. **110**, 014102 (2017).
[41] C. J. Naify, C. A. Rohde, T. P. Martin, M. Nicholas, M. D. Guild, and G. J. Orris, Generation of topologically diverse acoustic vortex beams using a compact metamaterial aperture, Applied Physics Letters **108**, 223503 (2016).
[42] H. Esfahlani, H. Lissek, and J. R. Mosig, Generation of acoustic helical wavefronts using metasurfaces, Phys. Rev. B **95**, 024312 (2017).
[43] J. B. Pendry, Negative refraction makes a perfect lens, Phys. Rev. Lett. **85**, 3966 (2000).
[44] N. Fang, H. Lee, C. Sun, and X. Zhang, Sub–diffraction-limited optical imaging with a silver superlens, Science **308**, 534 (2005).
[45] J. Li, L. Fok, X. Yin, G. Bartal, and X. Zhang, Experimental demonstration of an acoustic magnifying hyperlens, Nat. Mater. **8**, 931 (2009).
[46] G. Lerosey, J. De Rosny, A. Tourin, and M. Fink, Focusing beyond the diffraction limit with far-field time reversal, Science **315**, 1120 (2007).
[47] C. Shi, M. Dubois, Y. Wang, and X. Zhang, High-speed acoustic communication by multiplexing orbital angular momentum, Proc. Natl. Acad. Sci. U.S.A. **114**, 7250 (2017).
[48] X. Jiang, B. Liang, J.-C. Cheng, and C.-W. Qiu, Twisted acoustics: metasurface-enabled multiplexing and demultiplexing, Advanced Materials **30**, 1800257 (2018).
[49] X. Jiang, C. Shi, Y. Wang, J. Smalley, J. Cheng, and X. Zhang, Nonresonant metasurface for fast decoding in acoustic communications, Physical Review Applied **13**, 014014 (2020).
[50] X. Jiang, N. Wang, C. Zhang, X. Fang, S. Li, X. Sun, Y. Li, D. Ta, and W. Wang, Acoustic orbital angular momentum prism for efficient vortex perception, Applied Physics Letters **118**, 071901 (2021).
[51] P. J. Westervelt, Parametric acoustic array, Jour. Acous. Soc. Am. **35**, 535 (1963).
[52] H. Zhou, S. Huang, and W. Li, Parametric acoustic array and its application in underwater acoustic engineering, Sensors **20**, 2148 (2020).
[53] X.-D. Fan, Z. Zou, and L. Zhang, Acoustic vortices in inhomogeneous media, Physical Review Research **1**, 032014 (2019).
[54] T. Brunet, J.-L. Thomas, and R. Marchiano, Transverse shift of helical beams and subdiffraction imaging, Physical review letters **105**, 034301 (2010).
[55] L. Li and F. Li, Beating the rayleigh limit: Orbital-angular-momentum-based super-resolution diffraction tomography, Physical Review E **88**, 033205 (2013).
[56] W.-C. Lo, C.-H. Fan, Y.-J. Ho, C.-W. Lin, and C.-K. Yeh, Tornado-inspired acoustic vortex tweezer for trapping and manipulating microbubbles, Proceedings of the National Academy of Sciences **118** (2021).

[57] S. R. Sirsi and M. A. Borden, State-of-the-art materials for ultrasound-triggered drug delivery, Advanced drug delivery reviews **72**, 3 (2014).
[58] Y. Meng, K. Hynynen, and N. Lipsman, Applications of focused ultrasound in the brain: From thermoablation to drug delivery, Nature Reviews Neurology , 1 (2020).
[59] I. Basistiy, V. Y. Bazhenov, M. Soskin, and M. V. Vasnetsov, Optics of light beams with screw dislocations, Optics communications **103**, 422 (1993).
[60] K. Dholakia, N. Simpson, M. Padgett, and L. Allen, Second-harmonic generation and the orbital angular momentum of light, Physical Review A **54**, R3742 (1996).
[61] A. Berzanskis, A. Matijosius, A. Piskarskas, V. Smilgevicius, and A. Stabinis, Conversion of topological charge of optical vortices in a parametric frequency converter, Optics communications **140**, 273 (1997).
[62] A. Beržanskis, A. Matijošius, A. Piskarskas, V. Smilgevičius, and A. Stabinis, Sum-frequency mixing of optical vortices in nonlinear crystals, Optics communications **150**, 372 (1998).
[63] R. Marchiano and J.-L. Thomas, Doing arithmetic with nonlinear acoustic vortices, Physical review letters **101**, 064301 (2008).
[64] T. Brunet, J.-L. Thomas, R. Marchiano, and F. Coulouvrat, Experimental observation of azimuthal shock waves on nonlinear acoustical vortices, New Journal of Physics **11**, 013002 (2009).
[65] J.-L. Thomas, T. Brunet, and F. Coulouvrat, Generalization of helicoidal beams for short pulses, Physical Review E **81**, 016601 (2010).
[66] See Appendices A-B for more details about the design of the focused helical source and the experimental setup.
[67] See Appendix D for more details about the conservation of the topological charge of the self-demodulated vortex after the nonlinear mixing process.
[68] See Appendix C 1 for more details about the analytical model.
[69] P. Yuldashev and V. Khokhlova, Simulation of three-dimensional nonlinear fields of ultrasound therapeutic arrays, Acoust. Phys. **57**, 334 (2011).
[70] See Appendix C 2 for more details about the numerical method used for the nonlinear simulation of the acoustic vortices.
[71] See Appendix D for additional combinations of topological charges and frequencies.
[72] M. Baudoin, J.-C. Gerbedoen, A. Riaud, O. B. Matar, N. Smagin, and J.-L. Thomas, Folding a focalized acoustical vortex on a flat holographic transducer: miniaturized selective acoustical tweezers, Sci. Adv. **5**, eaav1967 (2019).
[73] A. D. Pierce, *Acoustics: An Introduction to Its Physical Principles and Applications* (Springer, 2019).

Appendix A: Helical source design

The generation of the two confocal primary vortex beams is based on a helical surface. The surface should produce the focusing of the acoustic waves at the focal point $\mathbf{r}(x, y, z) = \mathbf{r}(0, 0, F)$ and, simultaneously, a phase dislocation at this point. The time-of-flight at the focal spot should present an azimuthal dependence of the type

$$\Delta t_n(\phi) = \frac{l_n \phi}{\omega_n}, \tag{A1}$$

where l_n is the topological charge and ω_n the angular frequency of the n-th vortex beam and ϕ the azimuthal angle. To guarantee such phase, we design a helical surface as shown in Fig. 5. The surface design is constrained by the distance to the focal point, which must follows this relation

$$R_n(\phi) = F - \frac{l_n \lambda_n \phi}{2\pi}, \tag{A2}$$

at any point, where $\lambda_n = 2\pi c_0/\omega_n$. This surface, defined in spherical coordinates as $\mathbf{r} = \mathbf{r}(\phi, \theta, R_n(\phi))$, can be expressed in Cartesian coordinates as

$$x_n(\phi, \theta) = R_n(\phi) \cos(\phi) \sin(\theta), \tag{A3}$$
$$y_n(\phi, \theta) = R_n(\phi) \sin(\phi) \sin(\theta), \tag{A4}$$
$$z_n(\phi, \theta) = -[F + R_n(\phi) \cos(\theta)], \tag{A5}$$

where the azimuthal and elevation angles ranges between $0 < \phi < 2\pi$ and $\theta^{[n]}_{\min} < \theta < \theta^{[n]}_{\max}$, respectively. The aperture angles are given by

$$\theta^{[2]}_{\max} = \tan^{-1}\left(\frac{a}{2F}\right), \tag{A6}$$
$$\theta^{[2]}_{\min} = \tan^{-1}\left(\frac{a_h}{2F}\right), \tag{A7}$$
$$\theta^{[1]}_{\max} = \theta^{[2]}_{\min}, \tag{A8}$$
$$\theta^{[1]}_{\min} = 0, \tag{A9}$$

where $2a$ is the outer-source aperture and $2a_h$ is the aperture of the inner source.

Appendix B: Experimental methods

The two vortex sources were manufactured by placing two concentric arrays of transducers over the helical surfaces. Each of the sources was composed of two concentric arrays of piezoelectric transducers, as shown in Fig. 6. Each piezoelectric transducer (MA40S4S, Murata Manufacturing Co., Ltd.) presents an aperture of 10 mm and produces a sound pressure level of 120 dB SPL (0 dB = 20 μPa) measured at 30 cm in air when excited with a sinusoidal signal of 10 V. The source consisted in a total of 74 transducers (50 for the inner and 24 for the outer source). Transducers were connected in parallel. For the first source (inner array) the design frequency was $f_1 = 40$ kHz while for the second one (outer array) the frequency was $f_2 = 41$ kHz. The topological charges of the primary vortex beams were set to $l_1 = 1$ and $l_2 = 2$. Source aperture was $2a = 110$ mm ($2a_h = 60$ mm) and the focal was $F = 100$ mm.

Signals were generated using an arbitrary function generator (AFG3022B, Tektronix, Capitol, UK) and amplified by a 60-dB gain 100-W Power Amplifier (Type 2713,

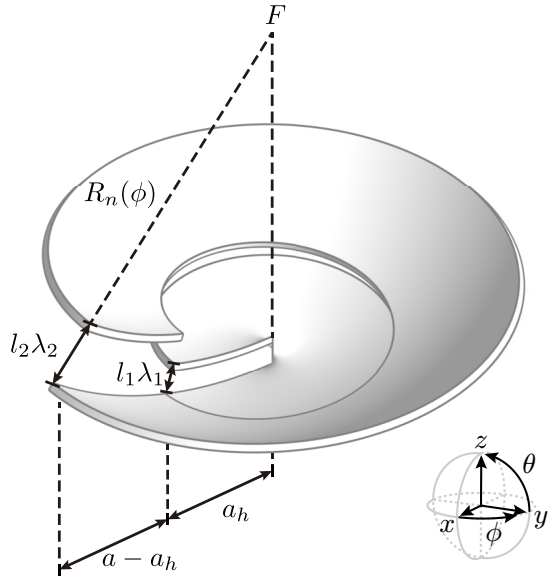

FIG. 5. Scheme of the helical surface to focus two confocal vortex beam.

Bruel & Kjaer, Naerum, Denmark). Each array was excited with a sinusoidal pulse burst of 4 ms duration. To guarantee a similar amplitude at the focal, the inner array and the outer array were excited with different amplitudes, 10 V and 12 V, respectively. This difference is likely due to the different number of transducers in each array presenting different impedances to the two amplifiers. These values were adjusted experimentally. Measurements were conducted in a semi-anechoic environment. Acoustic signals were acquired by using a 1/4-inch pressure-field microphone (G.R.A.S. Holte, Denmark) with a preamplifier (Type 26TC, G.R.A.S. Holte, Denmark) and signal conditioning module (12AQ, G.R.A.S. Holte, Denmark), and using a custom 2-mm diameter pinhole. Signals were acquired using a digitizer (Picoscope 5244B) with a sample-rate of 6.5 MHz. A total of 20 averages per measurement were performed to reduce noise.

The effect of the pinhole was evaluated experimentally by measuring the amplitude of an acoustic source at the axial direction using and without using the pinhole. Using the ultrasonic transducer as the source, we measure an attenuation of 18.7 dB for 40 kHz, and 19.15 dB for 41 kHz. Using a commercial electrodynamic loudspeaker, the measured attenuation was 0.026 dB at 1 kHz. At high frequencies the effect of the pinhole is important in terms of the measured amplitude, reducing the amplitude of the detected ultrasonic wave. However, at the self-demodulation frequency the sensibility of the microphone is not strongly affected, while the pinhole allows to scan the field with high spatial resolution.

The field was scanned using a 3D positioning system (Mistras NDT automation 1606). For the sagittal scans, $p = p(x, 0, z)$, the space was scanned using steps of 0.1 mm ranging for $30 < z < 180$ mm and $-20 < x < 20$ mm. For the transversal scans, $p = p(x, y, z_m)$, the space was scanned using steps of 0.1 mm ranging for $-20 < x < 20$ mm, $-20 < y < 20$ mm, at a height $z_m = 90$ mm that corresponds with the pressure maxima of the field. We note that the location of the pressure maxima does not correspond to the focus ($z_m < F$) due to wave diffraction.

Band-pass filtering was applied to show the demodulated signal in the time-domain by using a zero-gain zero-phase peak-filter. For the pressure field distributions the field amplitude at each component was calculated using fast-Fourier transforms.

Appendix C: Numerical methods

1. Linear regime: Rayleigh-Sommerfeld integral

The acoustic field at a point $\mathbf{r}$, generated by the radiating sources located along the helical surface was obtained using the Rayleigh-Sommerfeld integral, which can be written as

$$p(\mathbf{r}) = -i\frac{\rho_0 c_0 k}{2\pi}\int_{S_0}\frac{u_0(\mathbf{r_0})\exp(ik\,|\mathbf{r}-\mathbf{r_0}|)}{|\mathbf{r}-\mathbf{r_0}|}dS_0, \quad \text{(C1)}$$

were S_0 is the radiating surface of the sources located at $\mathbf{r_0}$. Each source vibrates with a particle-velocity of $u_0(\mathbf{r_0})$ normal to its surface S_0, moving at a frequency $\omega = c_0 k$ where k is the wavenumber, and ρ_0 and c_0 are the density and sound speed of the medium.

2. Nonlinear regime: Westervelt equation

The nonlinear field generated by the helical array source was approximated by the three-dimensional numerical integration of the second-order nonlinear wave equation in a thermoviscous fluid, also known as the Westervelt equation. We used the algorithm described and validated in Ref. [69]. In a retarded frame of coordinates such as $\tau = t - z/c_0$, with t the time and z the axial coordinate aligned with the beam, the one-way Westervelt equation is written as

$$\frac{\partial^2 p}{\partial\tau\partial z} = \frac{c_0}{2}\nabla^2 p + \frac{\beta}{2\rho_0 c_0^3}\frac{\partial^2 p^2}{\partial\tau^2} + \frac{b}{2\rho_0 c_0^3}\frac{\partial^3 p}{\partial\tau^3}, \quad \text{(C2)}$$

where p is the acoustic pressure, β is the coefficient of nonlinearity that for a gas is given by

$$\beta = \frac{\gamma+1}{2}, \quad \text{(C3)}$$

with $\gamma = C_P/C_V$ the ratio of specific heats or adiabatic index, b the thermoviscous absorption coefficient, given by

$$b = \zeta + \frac{4}{3}\eta + \kappa\left(\frac{1}{C_V} - \frac{1}{C_P}\right), \quad \text{(C4)}$$

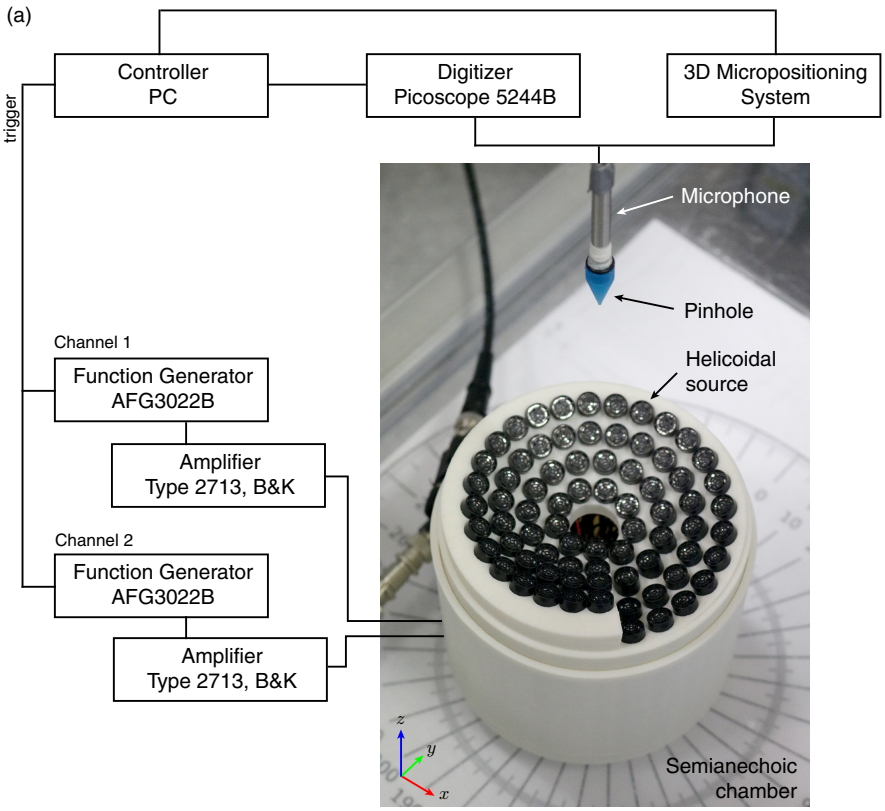

FIG. 6. Experimental setup.

with ζ and η the bulk and shear viscosities, κ the thermal conductivity, and C_P and C_V the specific heat at constant pressure and volume, respectively.

The numerical integration of Eq. (C2) is sequentially performed along the axial coordinate by using the operator-splitting technique. In the retarded coordinate frame the field $p(x, y, z, \tau)$ presents a small variation as compared with the field $p(x, y, z + \Delta z, \tau)$ for a small increment in axial coordinate, Δz. Therefore, we can split Eq. (C2) by its physical processes obtaining for the diffraction

$$\frac{\partial p}{\partial z} = \int \frac{c_0}{2} \nabla^2 p \, d\tau, \tag{C5}$$

for the nonlinearity

$$\frac{\partial p}{\partial z} = \frac{\beta}{2\rho_0 c_0^3} \frac{\partial p^2}{\partial \tau}, \tag{C6}$$

and for the absorption

$$\frac{\partial p}{\partial z} = \frac{b}{2\rho_0 c_0^3} \frac{\partial^2 p}{\partial \tau^2}. \tag{C7}$$

The field is expressed in the frequency domain by a finite Fourier series expansion, including N components as follows

$$p(x, y, z, \tau) = \sum_{n=-N}^{n=N} p_n(x, y, z) \exp(-i\omega_n \tau), \tag{C8}$$

where ω_n is the frequency of the n-th spectral component.

Using the operator-splitting technique, the field at a distance $z + \Delta z$ can be obtained as

$$p(z + \Delta z) = \Gamma_D^{[\Delta z/2]} \Gamma_N^{[\Delta z]} \Gamma_A^{[\Delta z]} \Gamma_D^{[\Delta z/2]} p(z), \tag{C9}$$

where $\Gamma_D^{[\Delta z/2]}$ approximates the diffraction given by Eq. (C5) over a distance $\Delta z/2$, $\Gamma_N^{[\Delta z]}$ approximates the nonlinearity given by Eq. (C6) over a distance Δz, and $\Gamma_A^{[\Delta z]}$ approximates the absorption given by Eq. (C7) over a distance Δz.

The diffraction operator given by Γ_D was calculated using the angular spectrum method by expanding the field $p_n(x, y)$ in the k-space $p_n(k_x, k_y)$ where

$$k_x = k_n \cos(\phi) \sin(\theta), \tag{C10}$$
$$k_y = k_n \sin(\phi) \sin(\theta), \tag{C11}$$

are the transversal components of the wavevector $k_n = \omega_n / c_0$. Thus, diffraction operator, applied in the k-space, is written as

$$\Gamma_D = \exp\left(i(k_z - k_n)\Delta z\right), \tag{C12}$$

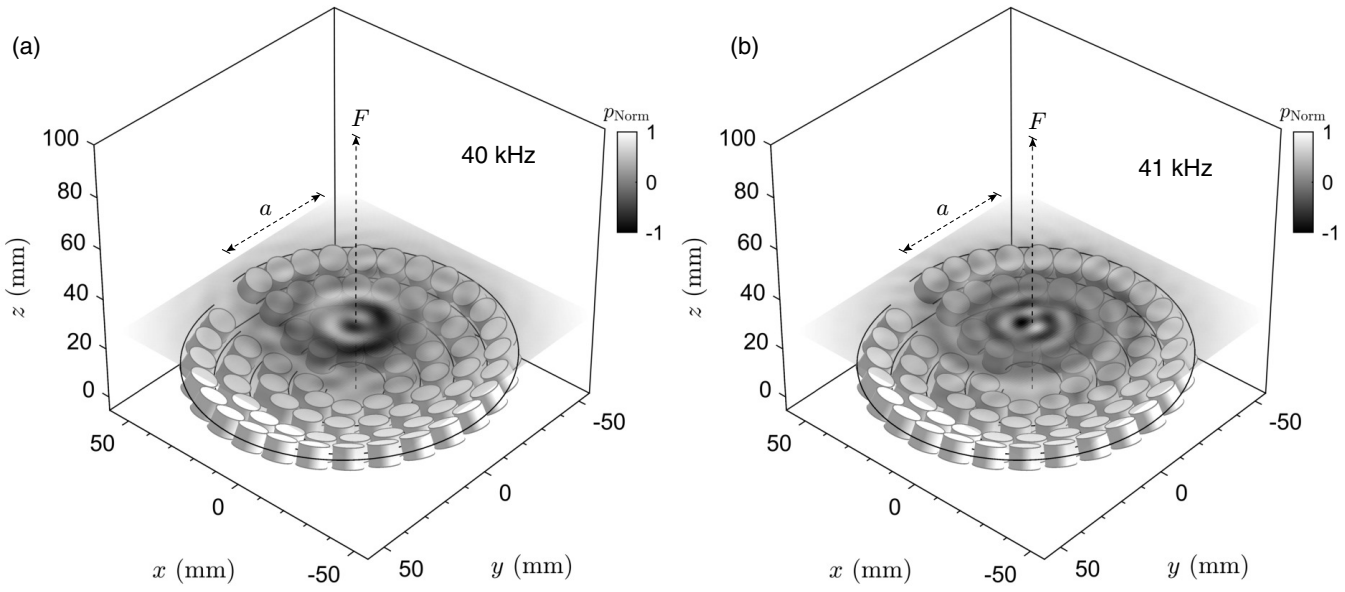

FIG. 7. Near-field integration for the sources using the Rayleigh-Sommerfeld equation used as the initial condition for the nonlinear simulations. (a) First source ($l_1 = 1$, $f_1 = 40$ kHz), (b) Second source ($l_2 = 2$, $f_2 = 41$ kHz).

with the axial component of the wavenumber given by

$$k_z = \sqrt{k_n^2 - k_x^2 - k_y^2}. \tag{C13}$$

As described in Ref. [69], k-space filtering and absorbing boundary conditions were used to avoid artificial wave reflections from the boundaries.

The nonlinear operator given by Γ_N was calculated by expressing Eq. (C6) in the frequency domain for a set of N spectral components as a set of nonlinear coupled equations

$$\frac{\partial p_n}{\partial z} = \frac{i\beta\omega_n}{\rho_0 c_0^3}\left(\sum_{k=1}^{N-n} p_k p_{n+k}^* + \frac{1}{2}\sum_{k=1}^{n-1} p_k p_{n-1}\right), \tag{C14}$$

where p_n^* is the complex conjugate of the harmonic amplitude p_n. Then, this equation is solved using a fourth order Runge-Kutta method for a step Δz.

Finally, assuming an exponentially decaying wave for a small Δz, the absorption operator was calculated using for the n-th spectral component

$$\Gamma_A = \exp\left(-\frac{b\omega_n^2}{2\rho_0 c_0^3}\Delta z\right). \tag{C15}$$

The initial conditions for the algorithm were set by integrating the field radiated for each source at a plane located at the exit of the array, $z = F - \sqrt{a^2 + F^2}$ using the Rayleigh-Sommerfeld integral given by Eq. (C1). We used 200 points to mesh the surface of each piezoelectric transducer. The initial conditions are shown in Fig. 7 for the two sources, each one being active at one frequency. Even in the near field, a phase dislocation is already visible at the axis.

For air at a temperature of $T = 20°$ C, we used the parameters [73] $\rho_0 = 1.21$ kg/m^3, $c_0 = 343$ m/s, $\gamma = 1.4$, $\zeta = 0.6\eta$, $\eta = 1.85 \times 10^{-5}$ Pa·s, $\kappa = 2.59 \times 10^{-2}$ W/mK and $C_P = 1.0061 \times 10^3$ J/kgK leading to $b = 4.6 \times 10^{-5}$ Pa·s and $\beta = 1.2$. The grid was set to $\Delta z = \lambda_d/240 = 1.4$ mm, the grid steps in the lateral dimensions was $\Delta x = \Delta y = \lambda_d/400 = 857$ μm, in domain given by $-2a < x < 2a$ and $-2a < y < 2a$, the number of the spectral components was $N = 120$ starting at $\omega_{n=1} = \omega_d$, i.e., the maximum frequency was 120 kHz.

Appendix D: Conservation of topological charge in self-demodulated vortices

The phase of the self-demodulated beam depends on the spatio-temporal interference of the two vortex beams, which is linked to their topological charges. In this section, we study the conservation of the topological charge by observing the generation of self-demodulated beams with a phase factor $\exp(il_d\phi)$. Due to the conservation of topological charge of nonlinear vortices, which is a consequence of the conservation of angular momentum, $l_d = s_d(l_2 - l_1)$ and $s_d = \text{sign}(\omega_2 - \omega_1)$ if the frequencies of the primary beams are non commensurate [22, 63], which is the common case in parametric acoustic antennas. Figure 8 shows the result of the phase of the self-demodulated beam at the focal spot for $-3, -2, \ldots, l_1, \ldots, 2, 3$ and $-3, -2, \ldots, l_2, \ldots, 2, 3$. We can see that the condition $l_d = l_2 - l_1$ is fulfilled for all cases, even when the two vortices collapse into a self-demodulated beam with no topological charge ($l_1 = l_2$).

It can be observed that when $||l_1| - |l_2|| \gg 0$ the quality of the synthesized vortex reduces because the field of the

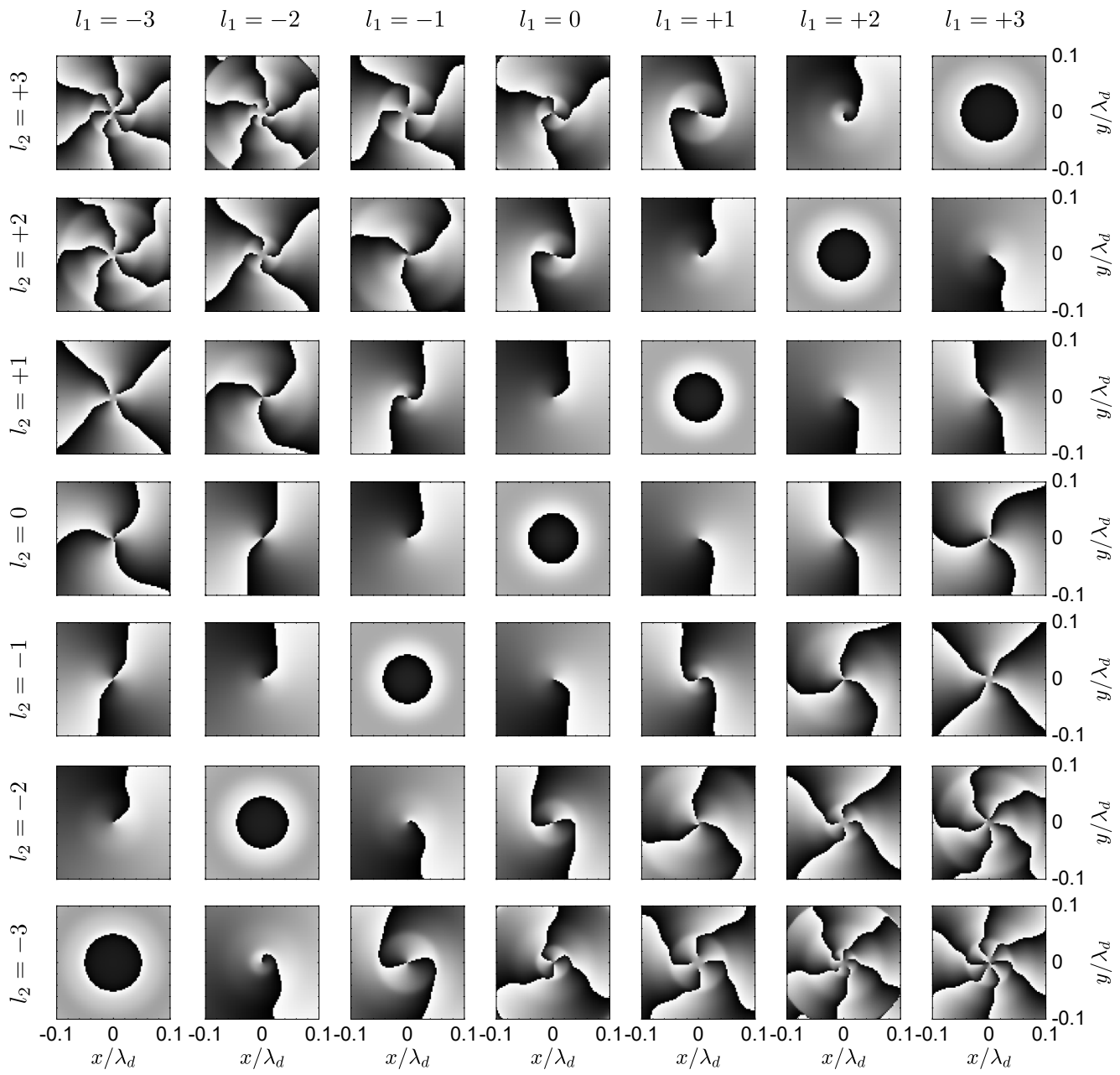

FIG. 8. Phase of the self demodulated beam as a function of the topological charges of the primary beams.

two primary beams does not fully overlap at the focal distance. In these cases, by tuning the aperture of each the primary beams, the radial component of the wavevector can be adjusted and, therefore, the width of the primary vortex beams can be adjusted to ensure that they overlap in space. In summary, to synthesise a sub-wavelength vortex by self-demodulation the primary beams should present different topological charge and their field distribution must overlap in space.

Another experimental setup was used to experimentally test the conservation of topological charge in self-demodulated vortices. The source elements of the first array are arranged in a flat circular shape, therefore $l_1 = 0$. It composed of $N_1 = 7$ identical transducers (MA40S4S, Murata Manufacturing Co., Ltd., Japan), working at a nominal frequency of 40 kHz. The second array consists of a helical surface with $N_2 = 12$ transducers with different heights h, as presented in Fig.9(a-b). The height of the n-th source is given by $h(n) = nl_i\lambda/N_i$, where N_i is the total number of transducers, and l_i the topological charge, $i = 1, 2$ for the i-th array. In our case, we used $l_2 = 1$, $\lambda = c_0/f_0 = 8.6$ mm, and $f_0 = 40$ kHz. Signals were generated using an arbitrary function generator (AFG3022C,Tektronix, Capitol, UK) and an ampli-

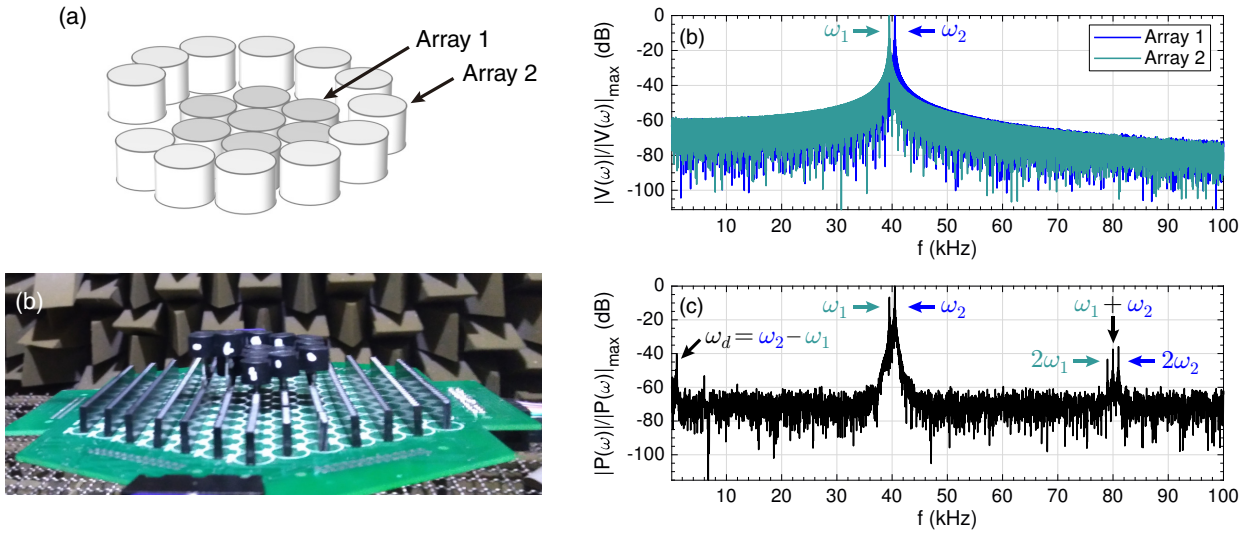

FIG. 9. (a) Scheme of the system composed of two arrays to generate divergent waves at frequencies ω_1, and ω_2. (b) Photograph of the array. (c) Normalized spectrum of the two excitation signals. (d) Normalized spectrum of the acoustic signal captured at the vortex focal spot.

fier to drive the two arrays. Each array was excited with a sinusoidal pulse burst of 14 ms duration. Both arrays were excited with the same amplitude, 5 V. Measurements were conducted in an anechoic chamber. Acoustic signals were acquired using an 1/8-inch calibrated microphone (G.R.A.S. Holte, Denmark), with a preamplifier and signal conditioning. Signals were acquired using an oscilloscope (GDS2104, Instek, Taipei,Taiwan) with a a sample-rate of 2 MHz. A XY-unit stage (Newmark Systems, Rancho Sta Marg, CA) was used to scan the acoustic field. Transverse planes were measured at $z = 190$ mm over a squared plane XY, -60 mm $\leq x \leq 60$ mm, and a step of $\Delta x = 2.5$ mm.

The primary frequencies used for each array were $f_1 = 39.5$ kHz, and $f_2 = 40.5$ kHz. The height of the helical source was estimated considering a frequency of 40 kHz, equivalent to the nominal frequency of transducers. With a frequency between 39 and 41 kHz, the helical array can generate acoustic vortices with minimal degradation since the height (pitch) of the source does not significantly change. Difference between the wavelength at 40 kHz and at ± 1 kHz is less than 3%. In this sense, we could excite the helical transducer at a range between 39 kHz and 41 kHz.

The spectrum of the input signals is presented in Fig. 9 (c), were only two components are observed at frequencies $f_1 = \omega_1/2\pi$, and $f_2 = \omega_2/2\pi$. On the other hand, the acoustic signal measured at $x = 0$ and $y = 2.5\lambda_1$ is shown in Fig. 9 (d), where besides the input frequencies, the first harmonics can be identified. In addition, the components $\omega_1 + \omega_2$, and $\omega_d = \omega_2 - \omega_1$ are presented in the frequency spectrum. The peak at ω_d is of the same order of magnitude as the first harmonics. Conversely, ω_d is two orders of magnitude (-40 dB) lower than the fundamental components.

Two experiments were performed using this setup. For the first experiment, we let the spherical wavefront ($l_1 = 0$) to interfere with the helical wavefront ($l_2 = 1$) leading

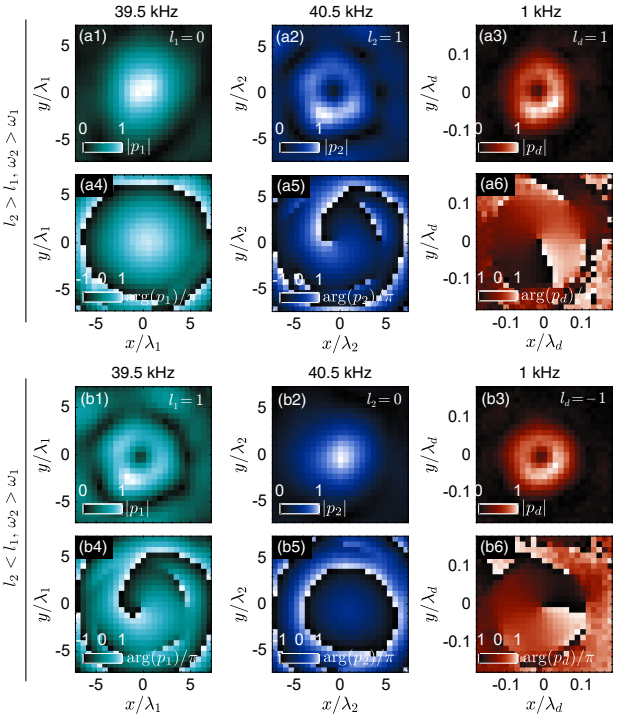

FIG. 10. Magnitude (a1, a2, b1, b2), and phase (a4, a5, b4, b5) of the primary beams and, magnitude (a3, b3), and phase (a6, b6) of the self-demodulated vortex beam, obtained experimentally.

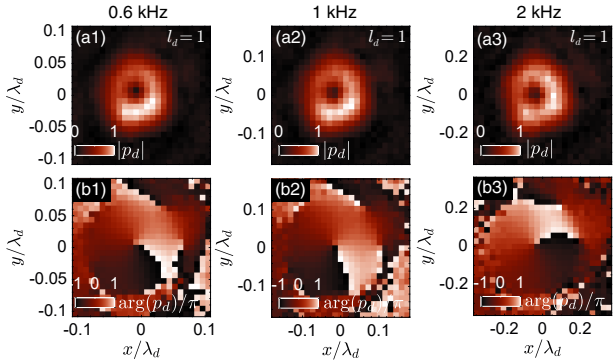

FIG. 11. Experimental results of the acoustic field at $z = 19$ mm, showing the magnitude (a1-a3), and phase (b1-b3) for self-demodulated vortex at 0.6 kHz, 1 kHz, and 2 kHz.

to a self-demodulated low-frequency helical beam. The self-demodulated vortex arises as a nonlinear mixing of the two primary waves, and due to the conservation of the topological charge. The topological charge of the self-demodulated beam is $l_d = l_2 - l_1 = 1$. Because $l_2 > l_1$, the handedness is clockwise and $l_d = l_2$, as shown in Figs. 10(a1-a6). The second experiment consists in using the same frequencies but switching the input signals between the two arrays. This is equivalent to $l_1 > l_2$, resulting in $l_d = l_2 - l_1 = -1$. Therefore, the handedness of the self-demodulated vortex is reversed because of the spatio-temporal interference of the two primary vortex beams, as shown in Figs. 10(b1-b6).

One more experiment was carried out using different primary frequencies $f_1 = [39, 39.5, 39.7]$ kHz, and $f_2 = [41, 40.5, 40.3]$, such that $f_d = [2, 1, 0.6]$ kHz. Results are presented in Fig. 11. As the changes in the frequency of the primary beams are small, the width of the primary beams remains almost constant. The magnitude of the field of the self-demodulated beams, presented in Figs. 11(a1-a3), show a ring-shaped structure whose diameters remains almost constant.

However, the frequency of those self-demodulated beams is very different, so the ratio between their width and their wavelength are 15.1, 7.8 and 4.6, respectively. Note these ratios are smaller than in the experiment discussed in the main manuscript of this article due to the lack of focusing of the secondary setup. On the other hand, the phase of the field of the self-demodulated vortices is presented in Figs. 11(b1-b3), showing a constant topological charge for all experiments.